Synthesis and photocatalytic oxidation properties of iron doped titanium dioxide nanosemiconductor particles

Xinyong Li,*[ab] Po-Lock Yue[b] and Charles Kutal[c]

[a] *School of Environmental Science & Engineering, Dalian University of Technology, Dalian, 116023, China*
[b] *Department of Chemical Engineering, The Hong Kong University of Science & Technology, Clear Water Bay, Kowloon, Hong Kong*
[c] *Department of Chemistry, University of Georgia, Athens, GA 30602, U. S. A*

Received* (*in Toulouse, France*) *19th February 2003, Accepted 14th May 2003
First published as an Advance Article on the web 7th July 2003

The structure, physical characteristics and selective photocatalytic oxidation properties of quantum confined nanosize iron doped TiO_2 (Q-TiO_2/Fe^{3+}) particles were studied by TG-DSC, XRD, DRS, EPR and Selective Oxidation Photocatalytic Measurements. It is shown that the solubility of iron in the obtained Q-TiO_2/Fe^{3+} nanoparticles is 1.0 atom% and the iron doping level has a great influence on the transformation of anatase to rutile (A-R). The quantum confined effect was observed for Q-TiO_2/Fe^{3+} nanoparticles. All of the samples have EPR Bulk-Fe^{3+} and Surf-Fe^{3+} signals, which are located in the bulk and surface of TiO_2 nanoparticles respectively. Quantitative EPR results indicate that the relative EPR intensity of these paramagnetic centers shows regular change with varying corresponding iron modification level. *In situ* EPR indicates that the photogenerated charge carrier (h^+, e^-) could be trapped by different Fe^{3+} sites simultaneously, *i.e.*, trapping of h^+ is due to Surf-Fe^{3+} sites at $g = 4.30$, whereas that of e^- is attributed to Bulk-Fe^{3+} sites at $g = 1.99$. Selective photocatalytic oxidation of cyclohexane into cyclohexanol with higher selectivity has been obtained by molecular oxygen activation over Q-TiO_2/Fe^{3+} nanoparticles under mild conditions. It is thought that the optical surface state of Q-TiO_2/Fe^{3+} nanoparticles play a key role in the selective photocatalytic oxidations.

Introduction

Photocatalysis has received enormous attention in recent years because of its potential application in environmental treatment and fine chemical synthesis.[1–9] It is known that under aqueous conditions, organic contaminants in wasted water can be degraded into CO_2 and H_2O *etc.*, whereas under dry organic solvent conditions, the organic substrate may be selectively oxidized into fine chemical products rather than complete mineralization.[10–12] For the latter case, it may be noticed that C–H bond activation leading to catalytic oxidation of hydrocarbons is one of the most challenging chemical problems, in addition to being of great practical importance. In terms of the oxidant, molecular oxygen (O_2) is clearly the most desirable due to its ready availability and high reduction potential. Up to now, there has been some progress in the field of oxidation of alkanes under mild conditions by molecular oxygen.[13,14] Recently, photocatalytic selective oxidation of cyclohexane into cyclohexanol with higher selectivity has been performed by molecular oxygen under UV irradiation and mild conditions by using nano-TiO_2 as photocatalyst.[15] However, in terms of solar energy utilization, there are still some shortcomings for the above-mentioned processes, such as low quantum efficiency and poor photosensitivity of TiO_2 to visible light. For nanosemiconductor photocatalysts, in order to increase the quantum yield and the spectra sensitivities, the e^-/h^+ recombination has to be reduced and the band gap has to be decreased. An effective strategy for achieving this goal is to introduce some defects into TiO_2 lattice through selective metal ion doping. Up to now, a number of dopants have been found to be effective to increase the quantum efficiencies of photocatalytic mineralization processes. However, to our knowledge, selective photocatalytic oxidation of alkanes by using iron doped TiO_2 as photocatalyst with molecular oxygen as oxidant under mild conditions have not been reported. Here, this paper deals with the preparation and characterization and selective photocatalytic oxidation properties of quantum confined iron doped TiO_2 (Q-TiO_2/Fe^{3+}) nanoparticles. It is shown that selective photocatalytic oxidation of cyclohexane into cyclohexanol with higher selectivity has been achieved with molecular oxygen over Q-TiO_2/Fe^{3+} nanoparticles under visible irradiation and mild conditions.

Experimental

Materials

Q-TiO_2/Fe^{3+} nanoparticles were prepared by the Sol–Gel method and were well characterized. The purity of the cyclohexane, cyclohexanol, and cyclohexanone was checked by gas chromatography. When needed, cyclohexane and acetonitrile were dried respectively over metallic sodium and CaH_2 or $CaCl_2$

Q-TiO_2/Fe^{3+} nanoparticle preparation

Q-TiO_2/Fe^{3+} nanoparticles were prepared by an acid-catalyzed Sol–Gel method and subsequently extracted from the solvent by means of a supercritical CO_2 drying strategy followed by annealing at 400 °C for 2 h. The Q-TiO_2/Fe^{3+} nanoparticles had nominal concentration of 0.05, 0.5, 1, 2 and 5 atom% of iron with respect to the molar percentage of titania (leading to samples denoted TF0.05, TF0.5, TF1, TF2 and TF5). The iron doped TiO_2 sol was prepared as

 DOI: 10.1039/b301998e

follows: A definite amount of titanium *n*-butoxide (A. R. Aldrich) was added dropwise to the solution of 30 ml anhydrous ethanol at 0 °C under vigorous stirring. Similarly, calculated iron nitrate (A. R. Aldrich) was dissolved in 30 ml anhydrous ethanol and it was mixed with the ethanolic solution of titanium *n*-butoxide dropwise under vigorous constant stirring. The mixed sols were kept stirring for 24 h and an aqueous solution of HNO_3 was added slowly over the course of 70 min into the well agitated system at room temperature. The iron doped TiO_2 aerogels were allowed to age in the mother liquor for at least twice the gelation time. In supercritical carbon dioxide drying,[16] alcohol from the structure of the alcogel was replaced by carbon dioxide at 40 °C and 100 bar. The extractor was completely filled with cold alcohol in order to minimize evaporation of the solvent from the alcogel and to avoid cracks developing during pressure build up. CO_2 was pumped into the extractor to a pressure above its critical pressure, that is, 100 bar. Before entering the extractor, CO_2 was heated to a temperature above its critical temperature, that is, 40 °C. During drying, the flow of CO_2 to the extractor was held constant at 0.50 kg h^{-1} and controlled independently of pressure. In the separator, the solvent was separated from carbon dioxide by expansion. When the solvent was completely replaced, the extractor pressure was slowly reduced to ambient pressure. The product aerogel was ground to < 100 mesh and heated in a tube furnace in flowing oxygen at 473–1023 K for 2 h, which was a standard calcination procedure. The aerogels turn black after few minutes of annealing at 473–673 K and regain their white color after additional annealing for 2 h at 673–1023 K which yields Q-TiO_2/Fe^{3+} nanoparticles with different modification levels.

Characterization of Q-TiO_2/Fe^{3+} nanoparticles

The thermal decomposition behavior of the gel-type precursor was monitored by a Dupont 9900 TG-DSC thermal analyzer. The crystal structure of the Q-TiO_2/Fe^{3+} photocatalysts was characterized using X-ray diffraction (XRD). The X-ray diffraction patterns were taken on a Rigaku/D/max γ B diffractometer using Cu Kα radiation. To study the electronic structure characteristics of nanoparticles, diffuse reflectance spectra (DRS) were measured in the range of 300–700 nm using a HITACHI UV 200-10 Spectrophotometer. $BaSO_4$ was used as the reference. Electron paramagnetic resonance (EPR) was used to investigate the surface chemistry of Q-TiO_2/Fe^{3+} nanoparticles and photoinduced redox processes as well as interfacial charge carrier (e^-, h^+) transfer properties. EPR spectra of all Q-TiO_2/Fe^{3+} nanoparticle samples were performed on a Varian E-115 spectrometer operating in the X-band ($\nu = 9.2$ GHz) with 100 kHz field modulations at 77 K. EPR parameters were calibrated by comparison with a standard Mn^{2+}/ZnS (106 line distance, 34.05 mT) and 2, 2-diphenyl-1-picryldrazyl (DPPH, 9.7×10^{15} spins, $g = 2.0036$). For the *in situ* EPR study of photoinduced redox processes and interfacial charge carrier (e^-, h^+) transfer properties of Q-TiO_2/Fe^{3+} samples, a typical sample of TF1 was degassed at room temperature (10^{-5} Torr) in a high vacuum cell fitted with one quartz window at one side. Irradiation was carried out with an oriel 150 W Xe lamp fitted with a high efficiency parabolic reflector. The irradiation from the Xe lamp passed through a water filter and a 400 nm cut off filter to remove the ultraviolet and infrared components of the light and was then focused onto the front face of the EPR sample cavity, from which the cover plate had been removed.

Evaluation of photocatalytic selective oxidation cyclohexane over Q-TiO_2/Fe^{3+} nanoparticles

The photocatalytic selective oxidation runs were carried out in a quartz reactor fitted with a gas inlet and outlet (50 ml capacity) at room temperature. Illuminations were provided by a 150 W Xe lamp. A water filter and 400 nm cut off filter were used to remove ultraviolet and infrared components respectively. The irradiated cross-section was 6 cm^2. Q-TiO_2/Fe^{3+} nanosamples (50 mg), cyclohexane (10 ml), acetonitrile (10 ml) were placed in the reactor and stirred with a magnetic stirrer. The oxygen gas was bubbled into the liquid phase at a flow rate of 20 ml min^{-1}. After 3 h, the dispersions were sampled (1 mL), centrifuged, and subsequently filtered through a Millipore filter (pore size, 0.22 μm) to separate Q-TiO_2/Fe^{3+} nanoparticles. The filtrates were then subjected to gas chromatography using a Shimadzu GC-16A gas chromatograph equipped with a flame ionization detector, using columns packed with Carbowax 20 M 5% on Chromosorb W-AW. The reaction products were determined by comparison of their retention times with those of authentic samples. The selectivity refers to the part that was oxidized and was calculated by integration of the three products (*i.e.*, cyclohexanol, cyclohexanone and carbon dioxide) from the GC results.

Results and discussion

The thermal behavior and crystal structure of Q-TiO_2/Fe^{3+} nanoparticles

The thermal behavior of iron doped TiO_2 aerogels was investigated with TG/DSC at temperatures ranging from room temperature to 500 °C. The TG/DSC patterns of 1 atom% iron doped TiO_2 typical aerogel are shown in Fig. 1. The TG-DSC endothermic peak at around 100 °C and the weight loss represents the dehydration and loss of residual solvent. The endothermic peak at 275 °C is attributed to the combustion of organic substances contained in the aerogel. The exothermic peak at 370 °C is considered to be the formation of anatase. The gel-type precursor remains amorphous up to 370 °C, which suggested that the crystallization is kinetically hindered due presumably to the integrity of the porous network arising from the supercritical CO_2 drying. The XRD patterns of Q-TiO_2/Fe^{3+} nanoparticles with modification levels ranging from 0.05 to 5.0 atom% (TF0.05 to TF5) prepared at low temperatures (450 °C) are shown in Fig. 2. It can be seen that only the pure anatase phase was detected for Q-TiO_2/Fe^{3+} nanoparticles with modification levels of 0.05, 0.5 and 1 atom% (TF0.05, TF0.5 and TF1). For samples with higher modification levels (TF2 and TF5), besides the detected anatase phase, two new phases were found. One is a rutile phase, the other can be ascribed to α-Fe_2O_3. The formation of an α-Fe_2O_3 phase may be attributed to the solubility of iron in TiO_2 matrix which is 1 atom%.[17] More iron doping may induce the dopant concentration to attain saturation in the inner surface of the titania framework and is followed by producing an isolated iron oxide phase at the surface of the TiO_2 nanoparticles. On the other hand, the emergence of the rutile phase reveals that doping favors the transformation of anatase to rutile (A–R), which further supports the conclusion that transition metal doping has a great influence on the A–R transformation

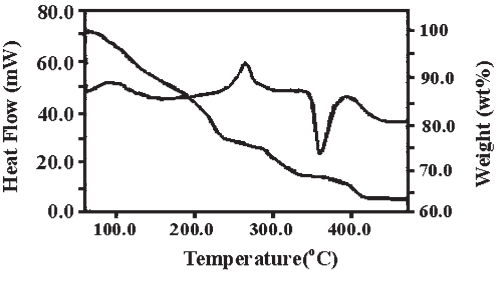

Fig. 1 The TG-DSC curve of iron doped TiO_2 aerogel.

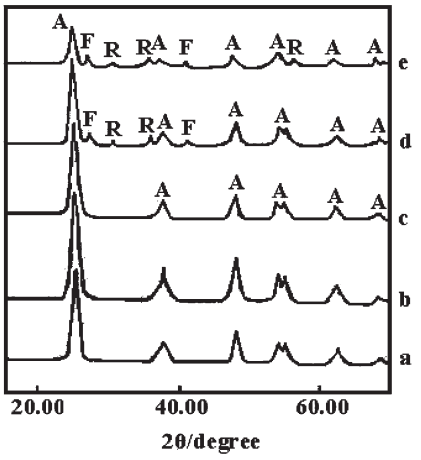

Fig. 2 X-Ray diffraction patterns (XRD) of Q-TiO_2/Fe^{3+} nanoparticles: (a) TF0.05, (b) TF0.5, (c) TF1, (d) TF2, (e) TF5.

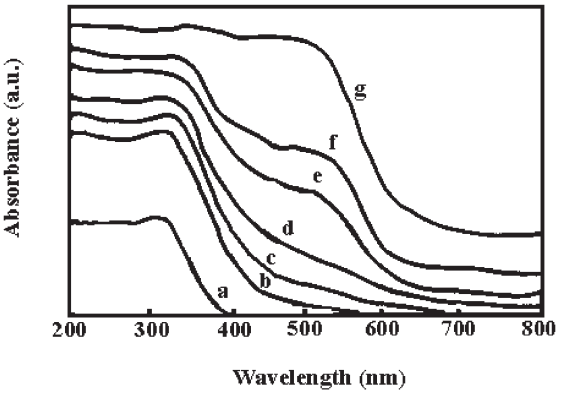

Fig. 3 Diffuse reflectance spectra (DRS) of Q-TiO_2/Fe^{3+} nanoparticles: (a) p-25 TiO_2, (b) TF0.05, (c) TF0.5, (d) TF1, (e) TF2, (f) TF5, (g) α-Fe_2O_3.

temperature of nano-TiO_2.[18] The XRD patterns also reveal that higher transition metal modification levels could cause the isolation of the iron oxide phase from TiO_2 matrix, which means more iron species may disperse on the surface of the TiO_2 matrix. The crystallite sizes of Q-TiO_2/Fe^{3+} nanoparticles as calculated from Scherrer's formula[19] are shown in Table 1. It is found that the crystallite size in the present investigation is in the range of 8.5–12.5 nm.

The electronic structure of Q-TiO_2/Fe^{3+} nanoparticles

Diffuse reflectance spectra (DRS) technique is a useful technique to characterize the electronic structure properties of nanoparticles. The DRS spectra of Q-TiO_2/Fe^{3+} nanoparticles with different modification level in comparison with p-25 TiO_2 and α-Fe_2O_3 are shown in Fig. 3. It is easily seen that p-25 TiO_2 shows an absorption threshold at *ca.* 380 nm and an $O_2 \rightarrow Ti^{4+}$ charge-transfer band with a maximum at around 325 nm. For Q-TiO_2/Fe^{3+} nanoparticles, the $O_2 \rightarrow Ti^{4+}$ charge-transfer band can be observed at *ca.* 310 nm. The onset of the absorption band is shifted towards lower wavenumbers with increasing modification level (460 nm for TF0.05 and 660 nm for TF5), *i.e.*, a red shift, which is attributed to the charge-transfer transition between the d electrons of the transition metal and the conduction band of the TiO_2 semiconductors. This red shift firmly attests the theory of the effect of quantum confinement of the nanoparticles, which could be explained with the Brus Theory.[20] From Fig. 3, it can be found that the TF0.05 sample with low iron content shows a constant absorption in the visible region higher than that of p-25 TiO_2. It may also be noticed that all of the Q-TiO_2/Fe^{3+} nanosamples show enhanced absorption in the range of 400–670 nm, increasing higher for higher iron doped samples and accompanying the change of color from white to red brown. The corresponding response of iron doped TiO_2 samples to visible light is very important for utilizing sunlight in photocatalytic reaction processes. For samples (TF2 and TF5) with higher iron modification levels, a broad band centered at *ca.* 530 nm can be observed. The spectra show typical features of minor amounts of α-Fe_2O_3, which is in good agreement with our XRD results.

Table 1 Characteristics of Q-TiO_2/Fe^{3+} nanoparticles prepared by the Sol–Gel method

Sample	D_p (atom%)[a]	T_{cal}/K[b]	D_{XRLB}/nm[c]	Phase[d]	Color
TF0.05	0.05	673	11.3	A	White
TF0.5	0.5	673	12.5	A	Buff
TF1	1.0	673	11.3	A	Yellow brown
TF2	2.0	673	11.3	A + R + F	Red brown
TF5	5.0	673	8.5	A + R + F	Red brown

[a] Iron doping level. [b] Calcination temperature. [c] Crystallite size calculated based on Scherrer's formula. [d] A: anatase R: rutile F: α-Fe_2O_3.

The surface state chemistry properties and light induced redox processes of Q-TiO_2/Fe^{3+} nanoparticles

EPR measurements of Q-TiO_2/Fe^{3+} nanoparticles with different modification levels as listed in Table 1 reveal that all of the samples have EPR signals. Typical EPR spectra are shown in Fig. 4. It can be seen from Fig. 4 that the EPR spectra are composed of two signals. EPR signal I at $g = 4.30$ is attributed to the Fe^{3+} (Surf-Fe^{3+}) dispersed on the surface of the TiO_2 nanoparticles, whereas EPR signal II at $g = 1.99$ can be assigned to Fe^{3+} (Bulk-Fe^{3+}) distributed in the bulk TiO_2 matrix.[21] The corresponding quantitative EPR results show that the relative EPR intensity of these two signals exhibits a smooth change with varying corresponding iron modification level. The quantitative EPR results are shown in Fig. 5. For all of the Q-TiO_2/Fe^{3+} nanosamples, it may be seen from Fig. 5 that the relative EPR intensity of Surf-Fe^{3+} on the TiO_2 surface is much lower than that of Bulk-Fe^{3+} in the TiO_2 matrix. While the iron modification level is less than 1 atom%, with increasing the iron content, the EPR intensity of Bulk-Fe^{3+} gradually increases and reaches a maximum value at 1 atom% iron modification level. This reveals that iron species may diffuse into the crystal lattice of TiO_2 to form a homogeneous solid solution as indicated from the XRD and DRS results. It may also reveal that, with increasing iron modification level, the relative EPR intensity of Surf-Fe^{3+}

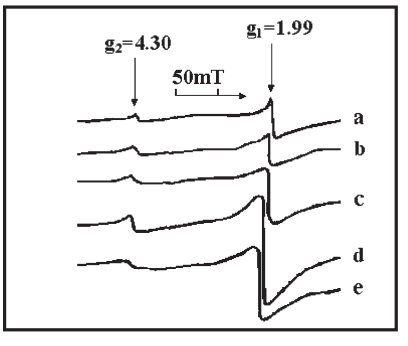

Fig. 4 Typical electron paramagnetic spectra (77 K) of Q-TiO_2/Fe^{3+} nanoparticles: (a) TF0.05 (b) TF0.5, (c) TF1, (d) TF2, (e) TF5.

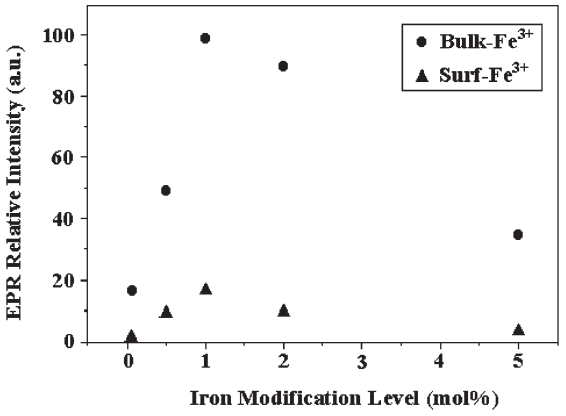

Fig. 5 The EPR characteristics of Q-TiO_2/Fe^{3+} nanoparticles with different modification levels.

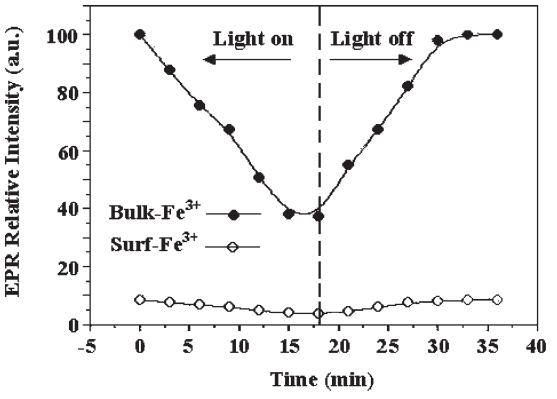

Fig. 7 *In situ* quantitative EPR characteristics of 1 atom% iron doped TiO_2 (TF1) nanoparticles with visible light irradiation time from 0 to 18 min at 77 K under vacuum conditions and after standing in the dark at 77 K for another 17 min.

increases correspondingly. This means that more iron species disperse on the surface of TiO_2 nanoparticles and thus induce the increase of the relative EPR intensity of Surf-Fe^{3+}. On the other hand, when the iron modification level is more than 1.0 atom%, the corresponding quantitative EPR results reveal that the EPR intensities of Surf-Fe^{3+} and Bulk-Fe^{3+} signals decrease with further increasing iron modification level. This may be caused by the agglomeration and separation of α-Fe_2O_3 species in the TiO_2 nanomatrix. EPR may not detect these agglomerated and isolated species.[22]

In order to check light induced redox processes and interfacial charge carrier (e^-, h^+) transfer characteristics, *in situ* EPR combined with white light irradiation (400–700 nm) are used to evaluate the processes. *In situ* EPR spectra obtained at 77 K on irradiation of a dry Q-TiO_2/Fe^{3+} nanosample (TF1) are shown in Fig. 6. The corresponding quantitative EPR results are given in Fig. 7. It was found that after performing irradiation for a period of time of 3, 6, 9, 12, 15 min and 18 min in vacuum (Fig. 6b, c, d, e, f and g), the EPR intensities of Bulk-Fe^{3+} and Surf-Fe^{3+} decreased correspondingly (see Fig. 7). The EPR signals decayed exponentially to 60% of their original intensity with a half-life of *ca.* 6 min, but no further changes occurred on prolonged irradiation. Also, no new EPR signals were detected on irradiation of Q-TiO_2/Fe^{3+} nanosamples. When the irradiation was stopped, the original spectrum was restored with a half-life of *ca.* 8.5 min (Fig. 6h, 6s). Compared with previous reports, the EPR intensity decrease of both Surf-Fe^{3+} and Bulk-Fe^{3+} EPR signals could

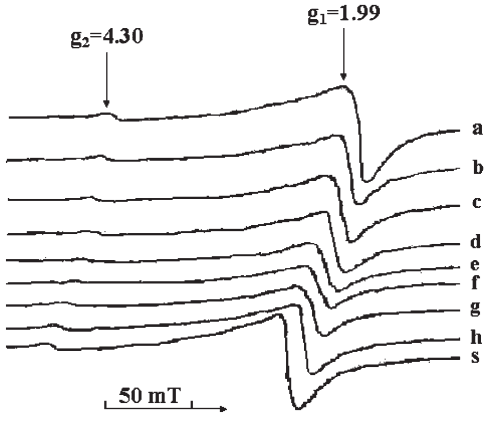

Fig. 6 EPR spectra of Q-TiO_2/Fe^{3+} (TF1) nanoparticles prior to and after visible light irradiation (VI) at 77 K under vacuum: 3×10^{-4} Torr: (a) prior to irradiation, (b) VI time (VIT) for 3 min, (c) VIT for 6 min, (d) VIT for 9 min, (e) VIT for 12 min, (f) VIT for 15 min, (g) VIT for 18 min, (h) Stop VIT for 10 min, (S) Stop VIT for 17 min.

be attributed to the trapping of charge carrier (h^+, e^-) by different Fe^{3+} sites simultaneously,[19b] *i.e.*, the trapping of h^+ for Q-TiO_2/Fe^{3+} nanoparticles is considered to be due to Surf-Fe^{3+} sites at $g = 4.30$, whereas that of e^- trapping can be though to occur at $g = 1.99$ of Bulk-Fe^{3+} sites. The fast separation of photogenerated charge carrier (h^+, e^-) and subsequent trapping simultaneously at different Fe^{3+} sites favor the surface–interface charge transfer of nano-semiconductor particles and thus increase of the photocatalytic efficiencies.

Selective photocatalytic oxidation of cyclohexane into cyclohexanol and cyclohexanone over Q-TiO_2/Fe^{3+} nanoparticles under mild conditions

The photocatalytic activity of selective oxidation of cyclohexane over Q-TiO_2/Fe^{3+} nanoparticles with different modification levels in comparison with p-25 TiO_2 under mild conditions are shown in Fig. 8a and 8b. For all samples, it was found from Fig. 8a that Q-TiO_2/Fe^{3+} photocatalysts with modification levels between 0.5 and 1 atom% iron content are relatively better catalysts, and the TiO_2 nanosample doped with 1 atom% iron is the best one. Compared with p-25 TiO_2, all of the doped nanosamples show higher catalytic activities for the selective photocatalytic oxidation of cyclohexane. When p-25 TiO_2 was used as the photocatalyst, cyclohexanone was the main product (the selectivity is *ca.* 82.5%) as indicated in Fig. 8b, which is in consistent with earlier reports.[23] However the situations are totally different when Q-TiO_2/Fe^{3+} nanoparticles were employed as catalysts and cyclohexanol is the main product (the maximum selectivity is *ca.* 81.6%) as shown in Fig. 8b. This reveals that further catalytic oxidation of cyclohexanol into cyclohexanone was greatly inhibited. Based on our XRD, DRS and EPR results, it is learned that the solubility of iron in TiO_2 nanoparticles matrix is 1.0 atom%, which is an important transforming point for the crystal structure, electronic structure and charge-trapping of iron doped TiO_2 nanoparticles. Both of the Surf-Fe^{3+} and Bulk-Fe^{3+} may act as catalytic centers with "shape selectivity" characteristics similar to that of zeolite.[24] The special surface state of the Q-TiO_2/Fe^{3+} nanoparticles could favor the selective oxidation of cyclohexane into cyclohexanol instead of cyclohexanone. It could also be noticed from Fig. 5 and Fig. 8a that with increasing iron modification level (modification level from 0.05 to 1.0 atom%), both the photocatalytic activities of iron doped TiO_2 samples and the EPR intensity of bulk-Fe^{3+} show similar change tendencies, *i.e.*, first increasing followed by attaining a maximum value and then decreasing with further increase of the iron doping level (iron content from 1.0 to 5.0 atom%). It is initially thought that Bulk-Fe^{3+}

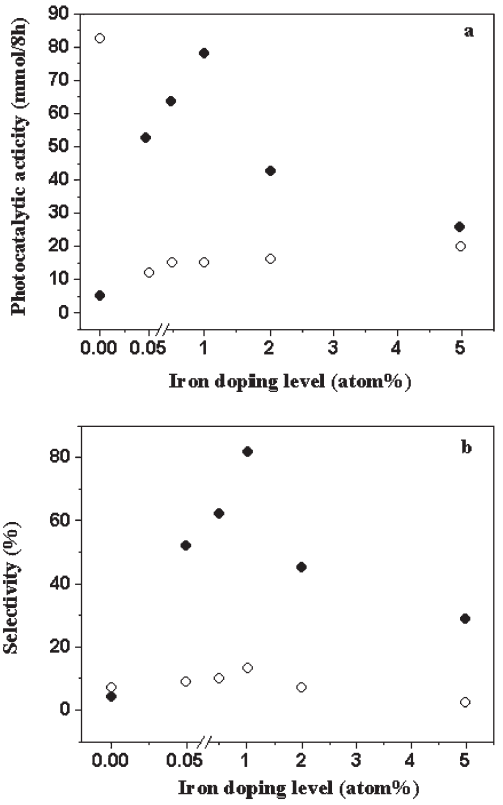

Fig. 8 The influence of iron doping level on (a) photocatalytic activity and (b) selectivity of catalytic oxidation of cyclohexane over iron doped TiO_2 nanoparticles (● Cyclohexanol, ○ Cyclohexanone).

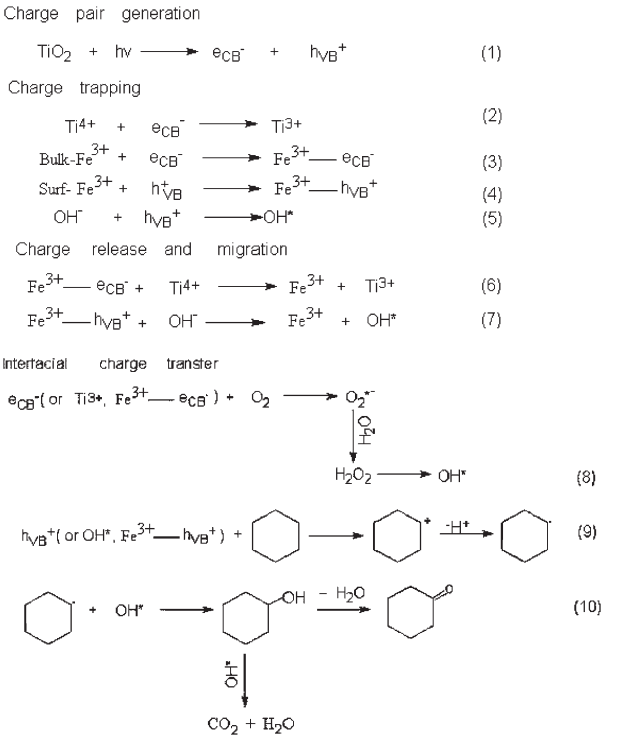

Scheme 1 Proposed mechanism of photo-induced redox processes and interfacial charge carrier transfer and mechanism of selective oxidation of cyclohexane by using molecular oxygen over Q-TiO_2/Fe^{3+} nanoparticles under mild conditions.

could trap the photogenerated electrons and then transfer them to pre-adsorbed species such as molecular oxygen on the surface of the Q-TiO_2/Fe^{3+} photocatalyst. Here, Bulk-Fe^{3+} may act as an "electron relay" and could achieve higher charge separation and surface–interface transfer efficiency. Detailed information on photo-induced charge carrier generation, separation, and interfacial transfer processes in Q-TiO_2/Fe^{3+} is given described in Scheme I.

While the iron modification level is less than 1 atom%, with increasing iron content, more and more iron species could diffuse homogeneously into the crystal lattice of titanium dioxide nanosamples as revealed by XRD. This means that more and more catalytic active centers and electron relay sites could be produced. The amount of these active centers would attain a maximum value on increasing the iron modification level to 1 atom%. Correspondingly, the catalytic activity and selectivity of selective photocatalytic oxidation of cyclohexane into cyclohexanol increased. This indicates that the optical surface state of Q-TiO_2/Fe^{3+} plays a key role in selective photocatalytic oxidation of alkanes. On the other hand, with further increasing the iron modification level, because of the limitation of solubility of TiO_2 nanoparticles, more and more iron species could not diffuse into the lattice of TiO_2 and may agglomerate at the surface of TiO_2 to form an isolated α-Fe_2O_3 phase. The two latter phases may induce the reducing of catalytic active centers and electron relay sites, which would have a negative influence on the photocatalytic selective oxidations.

Conclusions

Selective photocatalytic oxidation of cyclohexane into cyclohexanol with higher selectivity has been achieved by molecular oxygen activation under mild conditions over Q-TiO_2/Fe^{3+} nanoparticles. The crystal structure, electronic structure, EPR characteristics and interfacial charge transfer behavior were examined with XRD, DRS, and *in situ* EPR respectively. Some important results have been obtained. Q-TiO_2/Fe^{3+} nanoparticles with different modification levels have been synthesized by Sol–Gel methods combined with a supercritical CO_2 drying strategy. The XRD patterns of Q-TiO_2/Fe^{3+} indicate that an anatase phase could be produced at low temperatures (*i.e.*, 370 °C). The solubility of iron in the TiO_2 matrix is 1 atom%. More iron dopant modification level could cause the isolation of α-Fe_2O_3 and favor the transformation of anatase to rutile. The $O_2 \rightarrow Ti^{4+}$ charge-transfer bands were observed at *ca.* 310 nm for Q-TiO_2/Fe^{3+} nanoparticles. The quantum confined effect was observed for Q-TiO_2/Fe^{3+} nanoparticles. All of the samples have EPR signals that could be attributed to Bulk-Fe^{3+} and Surf-Fe^{3+} signals. The Bulk-Fe^{3+} and Surf-Fe^{3+} EPR paramagnetic centers are located in the bulk and surface of TiO_2 nanoparticles respectively. Quantitative EPR results show that the relative EPR intensity of Bulk-Fe^{3+} and Surf-Fe^{3+} signals exhibit regular change with varying corresponding iron modification level. *In situ* EPR irradiation results indicate that photo-generated charge carriers (h^+, e^-) could be trapped by different Fe^{3+} sites simultaneously, *i.e.*, trapping of h^+ is considered to be due to Surf-Fe^{3+} sites at $g = 4.30$, whereas that of e^- is ascribed to Bulk-Fe^{3+} sites at $g = 1.99$. Selective photocatalytic oxidation of cyclohexane into cyclohexanol with higher selectivity has been obtained by molecular oxygen activation over Q-TiO_2/Fe^{3+} nanoparticles under mild conditions. The photocatalytic activities show modification level and structure dependence. Bulk-Fe^{3+} could trap the photogenerated electrons and then transfer them to pre-adsorbed species such as molecular oxygen to form active oxygen species, whereas Surf-Fe^{3+} could trap holes. The charge carrier (h^+, e^-) trapping at different Fe^{3+} sites would greatly inhibit the recombination of photogenerated charge carriers and thus increase the efficiency of charge separation and interfacial charge transfer.

Acknowledgements

The author thanks Professor Dr Ralph Orga and Professor Dr Thomas Johnson for helpful discussions and kind advice.

References

1 A. L. Linsebigler, L. Guanquan and J. T. J. Yates, *Chem. Rev.*, 1995, **95**, 735–742.
2 Y. Mao and A. Bakac, *J. Phys. Chem.*, 1996, **100**, 4219–4226.
3 T. M. El-Morsi, W. R. Budakowski, A. S. Abd-El-Aziz and K. J. Friesen, *Environ. Sci. Technol.*, 2000, **34**, 1018–1022.
4 M. Miyauchi, A. Nakajima, A. Fujishima, K. Hashimoto and T. Watanabe, *Chem. Mater.*, 2000, **12**, 3–5.
5 J. Oh-Jin, *Proc. Natl. Acad. Sci. USA*, 2002, **99**, 6482–6486.
6 C. J. G. Cornu, A. J. Colussi and M. R. Hoffmann, *J. Phys. Chem. B*, 2001, **105**, 1351–1354.
7 R. R. Ozer and J. L. Ferry, *J. Phys. Chem. B*, 2000, **104**, 9444–9448.
8 A. Maldotti, L. Andreotti, A. Molinari, S. Borisov and V. Vasil'ev, *Chem. Eur. J.*, 2001, **7**, 3564–3571.
9 H. Einaga, S. Futamura and T. Ibusuki, *Appl. Catal. B: Environ.*, 2002, **38**, 215–225.
10 K. Wada, K. Yoshida, Y. Watanabe and T. Suzuki, *Appl. Catal.*, 1991, **74**, L1–L4.
11 T. Tanaka, T. Ito, S. Takenaka, T. Funabiki and S. Yoshida, *Catal. Today*, 2000, **61**, 109–115.
12 A. Maldotti, A. Molinari, A. Bergamini, R. Amadelli, P. Battioni and P. D. S. Mansuy, *J. Mol. Catal. A: Chem.*, 1996, **113**, 147–152.
13 K. I. Shimiz, T. Kaneko, T. Fujishima, T. Kodama, H. Yoshida and Y. Kitayama, *Appl. Catal. A: Gen.*, 2002, **225**, 185–191.
14 Li Xinyong and C. Kutal, *J. Mater. Sci. Lett.*, 2002, **21**, 1525–1527.
15 J. Li, X. Li and W. Li, *J. Jiangxi Normal Univ.*, 1997, **21**, 71–74.
16 Z. Novak, Z. Knez, M. Drofenik and I. Ban, *J. Non-Cryst. Solids*, 2001, **285**, 44–49.
17 A. R. Bally, E. N. Korobeinikova, P. E. Schmid, F. Levy and F. Bussy, *J. Phys. D: Appl. Phys.*, 1998, **31**, 1149–1154.
18 G. Cordoba, J. Padilla, V. H. Lara and R. Arroyo, *Mater. Lett.*, 2002, **54**, 397–402.
19 C. C. Wang and J. Y. Ying, *Chem. Mater*, 1999, **11**, 3113–3117.
20 Louis Brus, *J. Phys. Chem.*, 1986, **90**, 2555–2560.
21 M. Gratzael and R. F. Howe, *J. Phys. Chem.*, 1990, **95**, 274–279.
22 J. A. Navio, M. Macias, M. Gonzalez-Catalan and A. Justoo, *J. Mater. Sci.*, 1992, **27**, 3036–3041.
23 W. Mu, J. M. Herrmann and P. Pichat, *Catal. Lett.*, 1989, **3**, 73–76.
24 M. V. Landau, S. B. Kogan, D. Tavor, M. Herskowitz and J. E. Koresh, *Catal. Today*, 1997, **36**(4), 497–510.